

Article

Porous Rod-like NiTiO₃-BiOBr Heterojunctions with Highly Improved Visible-Light Photocatalytic Performance

Kaiyue Sun, Mengchao Li, Hualei Zhou *, Xiaohui Ma and Wenjun Li

Beijing Key Laboratory for Science and Application of Functional Molecular and Crystalline Materials, Department of Chemistry and Chemical Engineering, University of Science and Technology Beijing, Beijing 100083, China; sunkaiyue12345@163.com (K.S.); limengchao2020ks@163.com (M.L.); 18813010169@163.com (X.M.); wjli_ustb@163.com (W.L.)

* Correspondence: hlzhou@ustb.edu.cn

Abstract: NiTiO₃-BiOBr heterostructured photocatalysts were constructed via precipitation, calcination and hydrothermal treatments. Various characterizations demonstrated that BiOBr nanosheets were decorated on NiTiO₃ nanoparticles, forming porous rod-like heterojunctions. Compared with independent NiTiO₃ and BiOBr, the composites with optimal BiOBr content presented highly improved visible-light photocatalytic efficiency. The degradation rates of Rhodamine B (RhB) and tetracycline (TC) reached 96.6% in 1.5 h (100% in 2 h) and 73.5% in 3 h, which are 6.61 and 1.53 times those of NiTiO₃, respectively. The result is an improved photocatalytic behavior from the formation of heterojunctions with a large interface area, which significantly promoted the separation of photogenerated carriers and strengthened the visible-light absorption. Based on the free radical capture experiments and band position analysis, the photodegradation mechanism of type-II heterojunction was deduced. This study provides a new way to fabricate highly efficient NiTiO₃-based photocatalysts for degrading certain organics.

Keywords: photocatalysis; heterojunction; porous heterostructure; NiTiO₃; BiOBr



Citation: Sun, K.; Li, M.; Zhou, H.; Ma, X.; Li, W. Porous Rod-like NiTiO₃-BiOBr Heterojunctions with Highly Improved Visible-Light Photocatalytic Performance. *Materials* **2023**, *16*, 5033. <https://doi.org/10.3390/ma16145033>

Academic Editor: Davide Barreca

Received: 13 June 2023

Revised: 5 July 2023

Accepted: 12 July 2023

Published: 17 July 2023



Copyright: © 2023 by the authors. Licensee MDPI, Basel, Switzerland. This article is an open access article distributed under the terms and conditions of the Creative Commons Attribution (CC BY) license (<https://creativecommons.org/licenses/by/4.0/>).

1. Introduction

Currently, water pollution has become an increasingly serious environmental problem. Organic pollutants in wastewater discharged from factories or hospitals are usually hazardous to humans and difficult to remove [1,2]. Solar-driven photocatalytic technology has been deemed an environmentally friendly and effective technology employed for solving problems [3,4]. Many photocatalysts have been confirmed to be able to degrade organic pollutants, including colored dyes and uncolored organics with stable structures [5], but their photocatalytic efficiency has not been satisfactory for practical needs yet.

The perovskite oxide, NiTiO₃, has recently attracted large interest as a photocatalyst for degrading toxic pollutants due to its visible-light harvesting ability ($E_g = \sim 2.3$ eV), good electronic transportability and high stability [6–9]. Nevertheless, the photocatalytic activity of single NiTiO₃ is inhibited by severe recombination of photogenerated carriers and narrow light absorption range [10]. One of the most effective methods to overcome the problems is combining NiTiO₃ with other semiconductors with matched band structures to form various heterojunctions [11,12]. Among them, the staggered type-II heterojunction could not only notably accelerate the separation of the carriers but also extend/enhance the light absorption range. For instance, Shi et al. [11] fabricated Type II junctions between 2D Cu₂WS₄ nanosheets and 1D NiTiO₃ nanofibers, which exhibited excellent degrading ability for RhB and TC because of improved visible-light adsorption, rapid separation of photogenerated carriers and large specific surface area. Wang et al. fabricated type-II junctions composed of 3D NiTiO₃ nanorods and 2D MoS₂ nanosheets, which also notably inhibited the recombination of electrons and holes and presented high photocatalytic H₂

production [12]. Consequently, constructing efficient type-II heterojunctions is an ideal path to improving the photocatalytic performance of NiTiO_3 .

BiOBr is an efficient photocatalyst for degrading organic pollutants because of its strong oxidizing ability, lamellar structure and high chemical stability [13,14]. However, it suffers from the rapid combination of photoinduced carriers and poor visible-light absorption ($E_g \approx 2.7 \text{ eV}$) [15]. Therefore, BiOBr was often employed to construct heterojunctions with the visible-light-responsive semiconductor to enhance the solar photocatalytic property of the composites such as $\text{BiOBr-Bi}_2\text{WO}_6$ [16], $\text{BiOBr/Bi}_2\text{MoO}_6$ [17] and WS_2/BiOBr [18], profiting from the efficient separation of photo-induced carriers and improved visible-light absorption efficiency. Supposed that BiOBr and NiTiO_3 have matched band structures, $\text{NiTiO}_3\text{-BiOBr}$ heterojunctions would be expected to overcome their own shortcomings and exhibit high photocatalytic activity.

In addition, the photocatalytic behavior of the heterojunction also depends on the reasonable construction of the heterostructure, where there should be a large interface area and specific surface area for providing abundant active sites [19]. Consequently, employing the porous NiTiO_3 rods as supporters to in-situ grow the BiOBr nanosheets, the rod-like porous $\text{NiTiO}_3\text{-BiOBr}$ binary heterojunctions were fabricated through precipitation, calcinations and hydrothermal methods for the first time in this study. Rhodamine B (RhB) and tetracycline (TC) were separately employed as objects of photodegradation to evaluate the performance of the composites. As a result, the composites presented highly improved photocatalytic performances compared to the single components. The photocatalyst undoubtedly exhibited high stability. Furthermore, a feasible photocatalytic mechanism was deduced based on free radical capture, EPR tests and band position measurements. This study would present a new way to construct stable NiTiO_3 -based photocatalysts for degrading certain organics.

2. Experiments

2.1. Synthesis of NiTiO_3

NiTiO_3 was synthesized according to the method reported by Qu et al. [20], where 2.48 g of nickel acetate ($\text{Ni}(\text{CH}_3\text{COO})_2 \cdot 4\text{H}_2\text{O}$) was dissolved into 60 mL of ethylene glycol (EG) under stirring, and then 3.4 mL of tetra-n-butyl titanate ($\text{Ti}(\text{OC}_4\text{H}_9)_4$) was added dropwise in sequence. During this process, light blue precipitates were produced, which gradually increased in quantity. The reaction continued for 1 h. Subsequently, the precipitates were collected, washed with deionized water and ethanol in turn, and dried at 80°C . The resulting product was roasted in the air at 600°C for 2 h to attain yellow NiTiO_3 samples.

2.2. Synthesis of $\text{NiTiO}_3\text{-BiOBr}$ Composites

The $\text{NiTiO}_3\text{-BiOBr}$ composites were prepared by hydrothermal treatment. First, 0.1 g NiTiO_3 was added to 30 mL of deionized water under stirring to achieve a homogeneous suspension. Second, 10 mL of EG containing an appropriate proportion of $\text{Bi}(\text{NO}_3)_3 \cdot 5\text{H}_2\text{O}$ was added dropwise with stirring and then continuously stirred for an extra 30 min. Subsequently, a certain volume of $1 \text{ mg} \cdot \text{mL}^{-1}$ KBr solution was also added to it and fully mixed. The resulted mixture was placed into a Teflon-lined stainless autoclave (100 mL) and kept heating at 180°C for 12 h. As a result, the product was obtained by centrifugation, washed and dried as described above. The obtained products were named $\text{NiTiO}_3\text{-BiOBr}(x)$, in which x signifies the designed weight percentage of BiOBr in the composite (5 wt%, 10 wt%, 15 wt% and 20 wt%, respectively). As a control experiment, a single BiOBr was synthesized with the same procedure as above without the addition of a NiTiO_3 sample.

2.3. Characterization

X-ray diffraction (XRD) spectra were employed to detect the crystalline properties of the products and performed on the XRD instrument (D/MAX-RB, Rigaku, Japan). A scanning electron microscope (SEM) equipped with an energy-dispersive X-ray (EDX)

spectrometer (SU8010, Hitachi, Japan) was applied to determine the morphologies and elemental distribution on the surface of samples. A transmission electron microscope (TEM, F-20, FEI, USA) was employed to analyze the internal morphology of samples by observing TEM and high-resolution TEM (HRTEM) images. Pore structure was characterized using an instrument from Quantachrome NOVA 4200e (USA). To study the chemical components and oxidation states of elements in the materials, X-ray photoelectron spectra (XPS) were tested on an XPS instrument (EscaLab 250Xi, Thermo, USA). UV-visible diffuse reflectance spectra (UV-vis DRS) were applied to explore the light absorption of samples and carried out on a UV-vis spectrophotometer (T9s, Persee, China). To detect the separation efficiency of photogenerated carriers, the photoluminescence (PL) spectra were tested on a fluorescence spectrophotometer (F-7000, Hitachi, Japan). To determine the main free radicals in the photocatalytic system, an electron paramagnetic resonance (EPR) spectrometer (JES-FA200, JEOL, Japan) was employed to obtain the EPR spectra. An electrochemical workstation (5060F, RST, China) with a three-electrode cell system was applied to attain the Mott–Schottky plots to determine the flat band potentials of pristine semiconductors. A saturated calomel electrode (SCE) and Pt filament were employed as the reference and auxiliary electrodes, respectively. A certain amount of the sample was ultrasonically dispersed in the mixed solution of ethanol and Nafion and then coated into a circular trough on the ITO conductive glass, which was dried and used as the working electrode.

2.4. Photocatalytic Activity Experiments

The photocatalytic properties of the samples were evaluated by degrading RhB ($20 \text{ mg}\cdot\text{L}^{-1}$) and TC ($40 \text{ mg}\cdot\text{L}^{-1}$). A 400 W xenon lamp with a filter ($>420 \text{ nm}$) was used as a light source. Typically, a 30 mg sample was added to 30 mL of an aqueous solution containing the organic pollutant under stirring. The suspension was kept in the dark for 60 min to reach the adsorption-desorption balance. After the lamp was turned on, 3.0 mL of the suspension was taken out and centrifuged at regular intervals (30 min for RhB and TC). The concentrations C_t of RhB and TC were measured at 554 nm and 357 nm, respectively, on the T9s spectrophotometer. The value of C_t/C_0 could signify degradation efficiency. Here, C_0 and C_t mean the concentration at the initial time and a certain time, respectively.

3. Results and Discussion

3.1. XRD Analysis

The XRD spectra of the samples are shown in Figure 1. The pattern of single NiTiO_3 is well in line with the standard pattern (JCPDS 33-0960). The characteristic peaks at 24.13° , 33.09° , 35.66° , 40.85° , 49.45° , 54.02° , 62.45° and 64.07° correspond to crystalline planes (012), (104), (110), (113), (024), (116), (214) and (300), respectively. In comparison, the patterns of NiTiO_3 -BiOBr composites clearly show all these peaks. Besides, the peaks at 10.90° , 25.16° , 31.70° , 32.22° , 39.38° , 46.21° and 57.12° indexed to planes (001), (101), (102), (110), (112), (200) and (212) of BiOBr (JCPDS 09-0393), respectively, could be easily observed on the patterns of the composites with high BiOBr content (15% and 20%). With the decrease in BiOBr content, the intensity of these peaks gradually decreases or becomes invisible. These results suggest the successful synthesis of the NiTiO_3 -BiOBr composite.

3.2. SEM and TEM Analysis

Taking the NiTiO_3 -BiOBr (15%) composites as an example, the morphology of the prepared samples could be determined by SEM, TEM and HRTEM images. NiTiO_3 shows a rod-like shape with aspect ratio of $\sim 3\text{--}5$ (Figure 2a). It is also noted that a small number of irregular nanoparticles accumulates around the rods, which could be prompted by the growth of crystals during the roasting process [20]. Independent BiOBr is circular flakes with 150–300 nm in diameter (Figure 2b). The morphology of NiTiO_3 does not significantly change after combining with BiOBr (Figure 2c). From the TEM image (Figure 2d), it can be seen that the rod-like composite is made of many tiny nanoparticles and presents a

porous structure, which should have a large specific surface area and interface area. In the HRTEM image (Figure 2e), the lattice spacing of 0.27 nm is attributed to the (104) lattice planes of NiTiO_3 , and the lattice spacings of 0.23 and 0.18 nm correspond to the (112) and (104) planes of BiOBr sheets, respectively. This verifies the formation of the NiTiO_3 -BiOBr heterojunction.

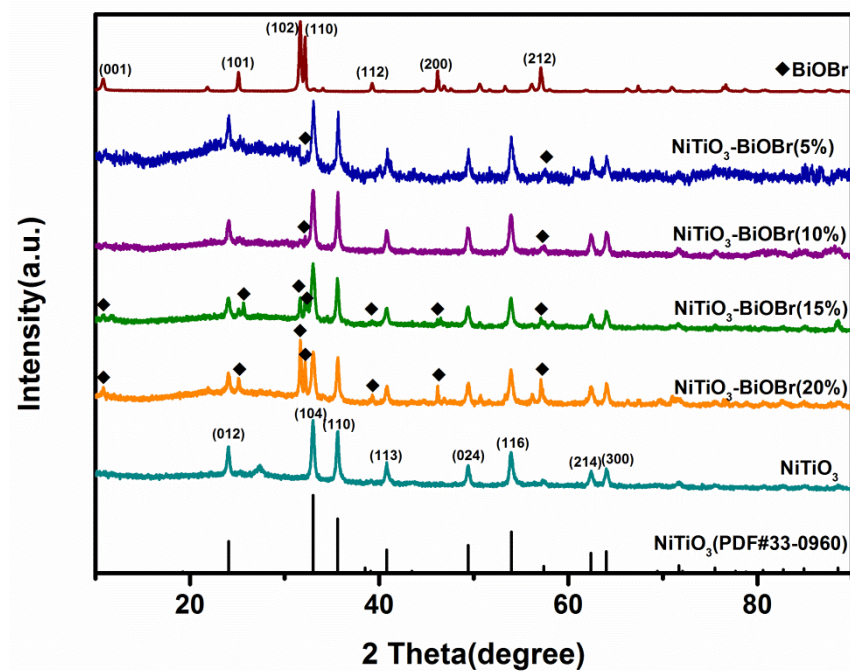


Figure 1. XRD patterns of the NiTiO_3 , BiOBr and NiTiO_3 -BiOBr composites.

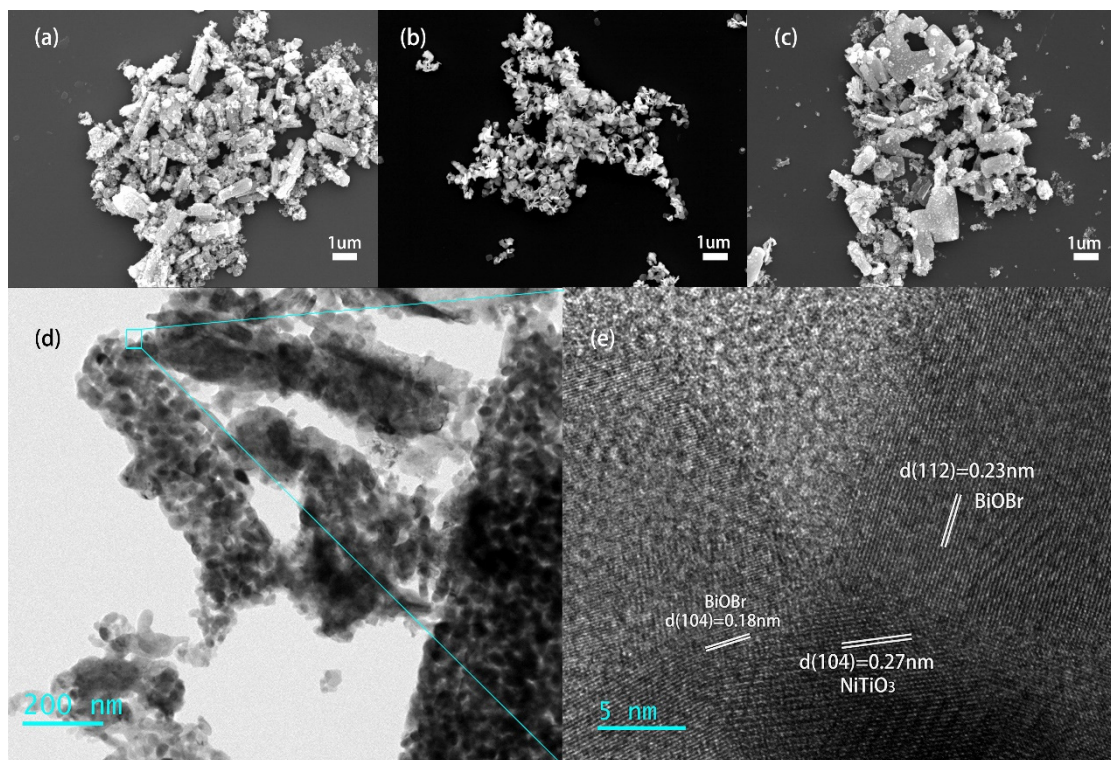


Figure 2. SEM pictures of (a) NiTiO_3 , (b) BiOBr, and (c) NiTiO_3 -BiOBr (15%) composites; (d) TEM image of NiTiO_3 -BiOBr (15%); (e) HRTEM image of NiTiO_3 -BiOBr (15%).

To illustrate the pore structure, N_2 adsorption isotherms and pore distributions of $NiTiO_3$ and $NiTiO_3$ -BiOBr (15%) are depicted in Figure 3a,b. Obviously, they belong to meso- and macro-pore structures with pore sizes of 50–150 nm, which leads to their large specific surface areas ($43.2\text{ m}^2\cdot\text{g}^{-1}$ for $NiTiO_3$, $33.0\text{ m}^2\cdot\text{g}^{-1}$ for the composite). The smaller surface area of the composite should result from the deposition of BiOBr, which blocked the partial pore of the $NiTiO_3$ rod. These results indicate that the composite has many abundant active sites and large interface area, which would be very beneficial for the photocatalytic process.

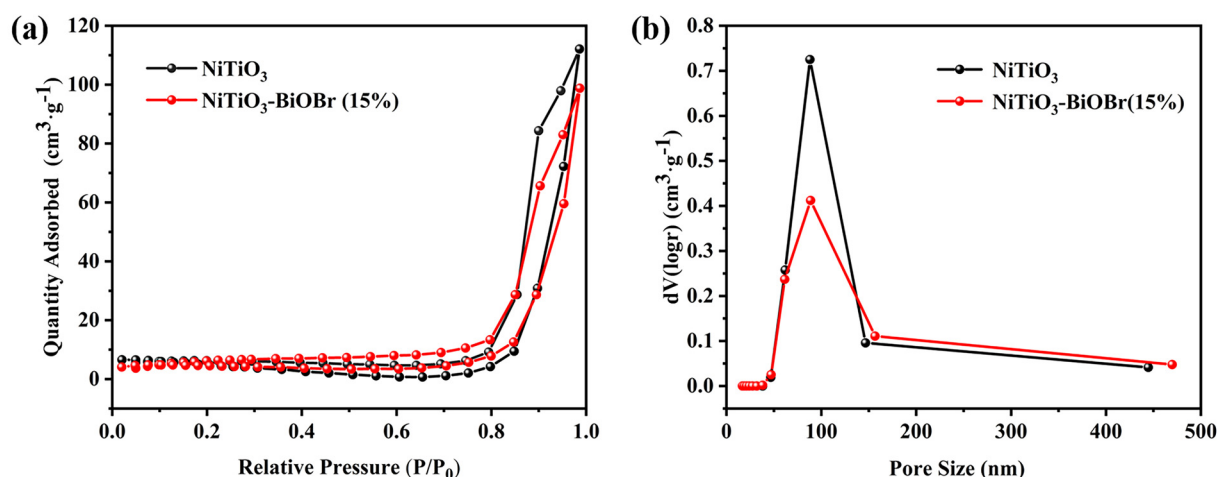


Figure 3. The N_2 adsorption isotherms (a) and pore distributions (b) of $NiTiO_3$ and $NiTiO_3$ -BiOBr (15%).

3.3. XPS Analysis

The chemical composition and elemental oxidation states of the composites were further examined by XPS. The characteristic peaks of Ni, Ti, Bi, O and Br elements could be obviously detected on the full survey spectra of $NiTiO_3$ -BiOBr (15%) (Figure 4a), indicating that these elements coexist in the binary composites. The spectrum of Ni 2p (Figure 4b) was fitted into two groups of peaks separately for both $NiTiO_3$ and binary composites, where the strong peaks at 855.33 and 872.72 eV are related to Ni 2p_{3/2} and Ni 2p_{1/2} of Ni^{2+} , respectively, and the other two weak peaks at 861.32 and 879.52 eV should be attributed to their satellite peaks [21]. Two obvious peaks of Ti 2p at 457.88 and 463.70 eV are assigned to the Ti 2p_{3/2} and Ti 2p_{1/2} of Ti^{4+} in $NiTiO_3$, respectively (Figure 4c) [21]. In Figure 4d,e, the peaks at 158.89 and 164.23 eV correspond to the Bi 4f_{7/2} and Bi 4f_{5/2} of Bi^{3+} , respectively, and the peaks at 67.58 and 68.78 eV ascribe to Br 3d_{5/2} and Br 3d_{3/2} of Br^- , separately [22,23], indicating the existence of the BiOBr component. For the O 1s spectra in Figure 4f, the peaks at 529.78 and 531.33 eV attribute to the O^{2-} of Bi-O bonds and adsorbed oxygen on the spectrum of single BiOBr, respectively [16], while the peaks at 529.65 and 531.20 eV designate the lattice O^{2-} in $NiTiO_3$ and the surface-adsorbed oxygen on the spectrum of $NiTiO_3$, respectively [24]. In comparison, the peak at 529.63 eV on the spectrum of the binary composites should be lattice O^{2-} in $NiTiO_3$ and BiOBr, while the peak at 530.86 eV could belong to the adsorbed oxygen. Apparently, the results further suggest the successful preparation of the $NiTiO_3$ -BiOBr heterojunction.

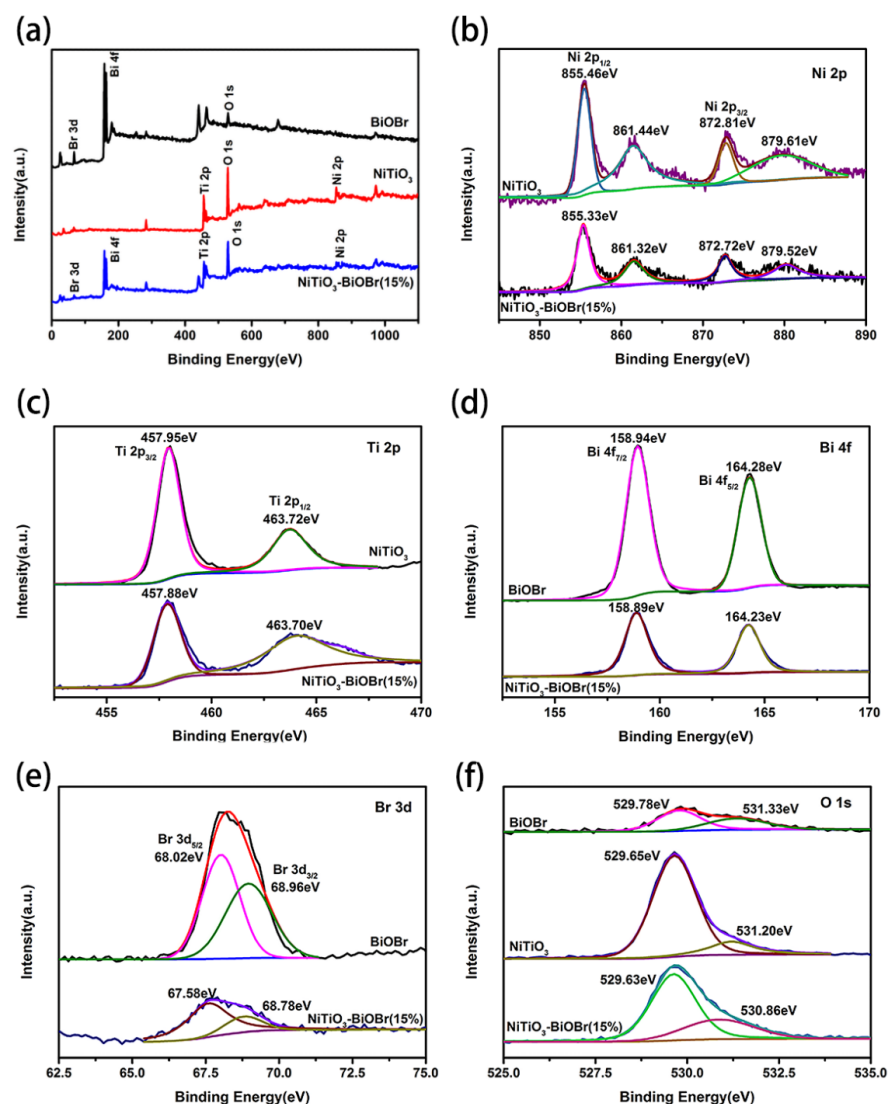


Figure 4. XPS analysis portraying NiTiO_3 , BiOBr and $\text{NiTiO}_3\text{-BiOBr}$ (15%): (a) Survey; (b) Ni 2p; (c) Ti 2p; (d) Bi 4f; (e) Br 3d; (f) O 1s.

3.4. Photocatalytic Properties

As shown in Figure 5a, only 14.6% and 49.0% of RhB within 1.5 h were degraded under visible-light irradiation over pristine NiTiO_3 and BiOBr , respectively. All binary materials, comparatively, exhibit higher degradation abilities for RhB. Among them, $\text{NiTiO}_3\text{-BiOBr}$ (15%) presents the highest efficiency, i.e., 96.6% within 1.5 h (100% within 120 min), which is 6.61 times that of pure NiTiO_3 . This indicates that the photocatalytic activity of NiTiO_3 in RhB degradation is amazingly boosted after coupling with an appropriate quantity of BiOBr , and the constructed $\text{NiTiO}_3\text{-BiOBr}$ heterojunction is highly efficient. Compared with other reported NiTiO_3 -based photocatalysts for degrading RhB, the $\text{NiTiO}_3\text{-BiOBr}$ photocatalyst presents notably high degradation efficiency in 90 min even if high concentration of RhB was used in this work (Table 1). The photodegradation of TC over the materials was further tested. As shown in Figure 5b, the composites also exhibit much higher activity in degrading TC than pristine NiTiO_3 and BiOBr . The $\text{NiTiO}_3\text{-BiOBr}$ (15%) composite also has the highest photodegradation rate (73.5%) within 3 h, which is far higher than NiTiO_3 .

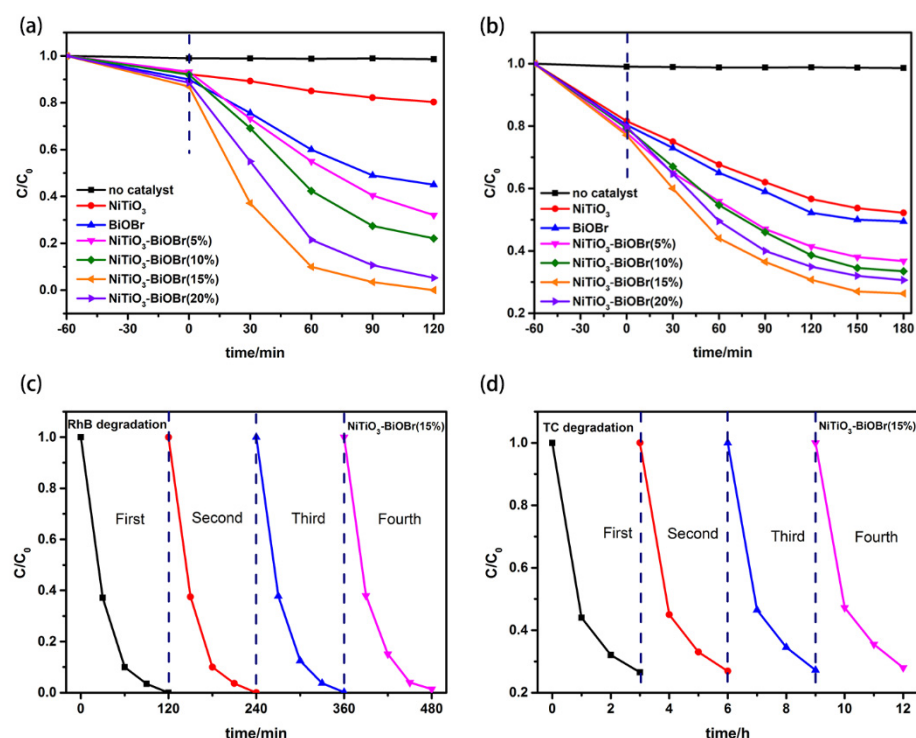


Figure 5. Photocatalytic degradation of prepared photocatalysts in degrading RhB (a) and TC (b); cycling tests of degrading RhB (c) and TC (d).

Cycling experiments over NiTiO₃-BiOBr (15%) for RhB and TC degradation were conducted to evaluate the stability of the materials. From Figure 5c,d, it is observed that the photocatalytic rate is basically unchanged after four repeated experiments, no matter what is degraded. Therefore, the stability of the binary composites is sufficient for the practical needs of photocatalytic systems.

Table 1. Comparison in the photodegradation performance for RhB among NiTiO₃-based photocatalysts.

Photocatalysts	C ₀ /mg·L ⁻¹	Time/min	Dosage of Catalyst/g·L ⁻¹	Efficiency/%	Refs.
NiTiO ₃ -Bi ₄ NbO ₈ Cl	5	90	1.0	~50	[24]
NiTiO ₃ -GO	10	90	0.2	~90	[25]
NiTiO ₃ -TiO ₂	-	90	1.0	~62	[26]
NiTiO ₃ -Bi ₂ MoO ₆	10	90	0.6	~92	[27]
NiTiO ₃ -α-Fe ₂ O ₃	3	90	0.1	~75	[28]
NiTiO ₃ -ZnO	5 ppm	120	0.5	95	[29]
NiTiO ₃ -BiOBr	20	90	1.0	96.6	This work

3.5. Photocatalytic Mechanism Discussion

3.5.1. UV-Vis DRS Analysis

The UV-Vis DRS of the samples is employed to analyze their optical absorption. As shown in Figure 6a, NiTiO₃ exhibits absorption ability in both the ultraviolet and visible light ranges. An obvious absorption peak is observed near 450 nm. According to the literature [11,20,21], crystal field splitting of the Ni-O octahedron in NiTiO₃ crystal causes the 3d⁸ orbits of Ni²⁺ to split up into two sub-bands, and the Ni²⁺/Ti⁴⁺ charge-transfer could lead to the formation of two adsorption peaks at ~450 and ~510 nm (not clear), respectively. In addition, NiTiO₃ also has light response above 600 nm due to the spin-allowing d-d transitions of Ni²⁺ [30]. In contrast, BiOBr mainly absorbs ultraviolet light and has an absorption edge of ~430 nm. By coupling them together, the composites present

a notably strong visible-light absorption characteristic compared to pristine NiTiO_3 and BiOBr .

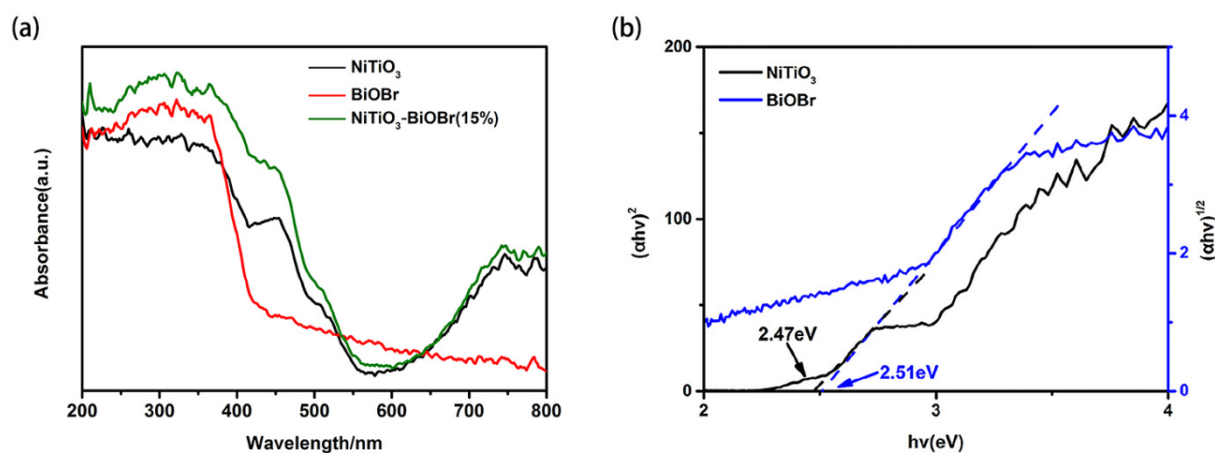


Figure 6. (a) UV-Vis DRS of NiTiO_3 , BiOBr and $\text{NiTiO}_3\text{-BiOBr}$ (15%) samples and (b) Tauc's plots of NiTiO_3 and BiOBr .

The band gaps of the two pristine samples were determined based on the equation: $(\alpha h\nu)^{2/n} = h\nu - E_g$, where α , h , ν , $h\nu$ and E_g represent absorbance coefficient, plank constant, light frequency, irradiation energy and band gap energy, respectively [31]. Here, n is 1 for NiTiO_3 (direct bandgap) [26] and 4 for BiOBr (indirect bandgap) [32]. Therefore, the E_g of NiTiO_3 and BiOBr was separately determined to be 2.47 and 2.51 eV, respectively (Figure 6b).

3.5.2. PL Emission Spectra

The function of the heterojunctions in inhibiting the recombination of photogenerated carriers can be revealed by PL spectra. In Figure 7, the composites present much lower peak intensities than single NiTiO_3 and BiOBr , indicating that the formation of heterojunction greatly inhibited the recombination of photogenerated carriers and prompted the separation of the carriers. Among them, $\text{NiTiO}_3\text{-BiOBr}$ (15%) presents the lowest peak intensity, implying its highest separation efficiency of carriers, which corresponds to its best photocatalytic performance.

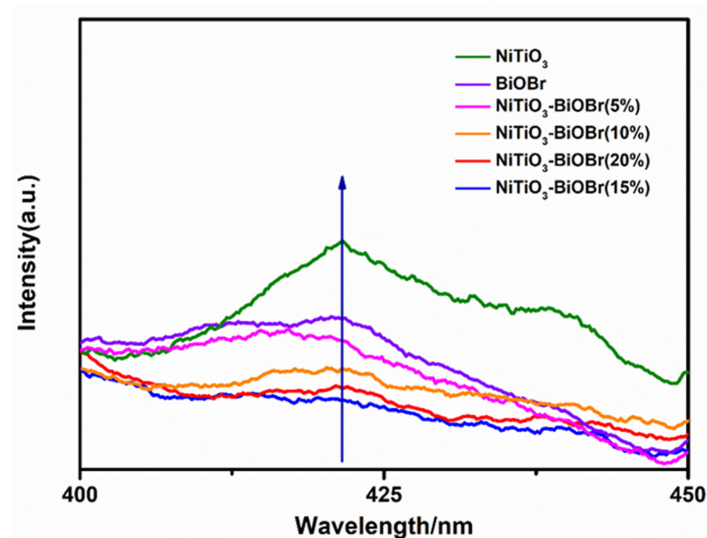


Figure 7. PL spectra of the samples at 280 nm of the light excitation wavelength (the arrow means the direction in which the peak values increase).

3.5.3. Free Radical Capture Tests

Hydroxyl radicals ($\cdot\text{OH}$), superoxide radicals ($\cdot\text{O}_2^-$) and holes (h^+) are usually responsible for the degradation of organics. Free radical capture tests were performed for the $\text{NiTiO}_3\text{-BiOBr}$ (15%) composite to investigate the degradation mechanisms of RhB and TC. $\text{Na}_2\text{C}_2\text{O}_4$ (10 mM), isopropanol (IPA, 10 mM) and benzoquinone (BQ, 1 mM) act as scavengers for h^+ , $\cdot\text{OH}$ and $\cdot\text{O}_2^-$, respectively. It is seen from Figure 8a that the photodegradation efficiency of RhB over $\text{NiTiO}_3\text{-BiOBr}$ (15%) mildly decreases after adding IPA but significantly decreases after the addition of $\text{Na}_2\text{C}_2\text{O}_4$ or BQ, implying that h^+ and $\cdot\text{O}_2^-$ are the main free radicals, while $\cdot\text{OH}$ has little contribution to the RhB degradation. For TC (Figure 8b), the degradation drastically decreases to near zero after adding BQ and also clearly declines when IPA is added, while there is little change after adding $\text{Na}_2\text{C}_2\text{O}_4$. This demonstrates that $\cdot\text{O}_2^-$ and $\cdot\text{OH}$ play key roles in the following order: $\cdot\text{O}_2^- > \cdot\text{OH}$, while h^+ hardly contributed to the degradation of TC, possibly due to its relatively low oxidability.

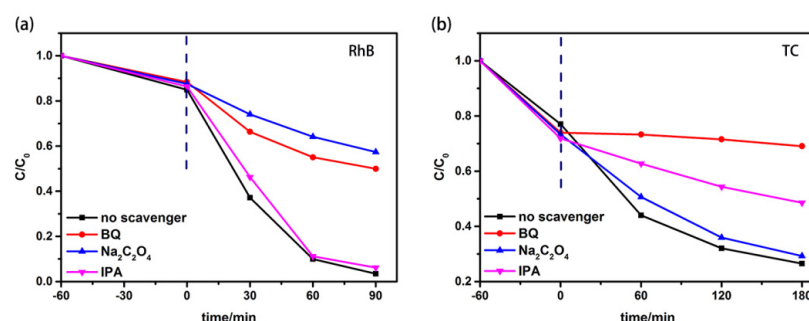


Figure 8. Degradation of RhB (a) and TC (b) over $\text{NiTiO}_3\text{-BiOBr}$ (15%) with different scavengers under visible-light irradiation.

EPR measurements were performed to further explore the change of free radicals with the formation of heterojunctions. In Figure 9a, the $\cdot\text{OH}$ signal in the $\text{NiTiO}_3\text{-BiOBr}$ composite system is hardly observed, while a weak signal could be detected in the single NiTiO_3 system, indicating that the heterojunction does not promote or is adverse to the formation of $\cdot\text{OH}$. In contrast, the $\text{DMPO}\cdot\text{O}_2^-$ signals can be explicitly detected. Additionally, the composite system exhibits a stronger signal than the single NiTiO_3 system (Figure 9b). This suggests that the heterojunction facilitates $\cdot\text{O}_2^-$ production, which is consistent with the results of the capture tests and show that $\cdot\text{O}_2^-$ plays a key role in the photocatalytic process.

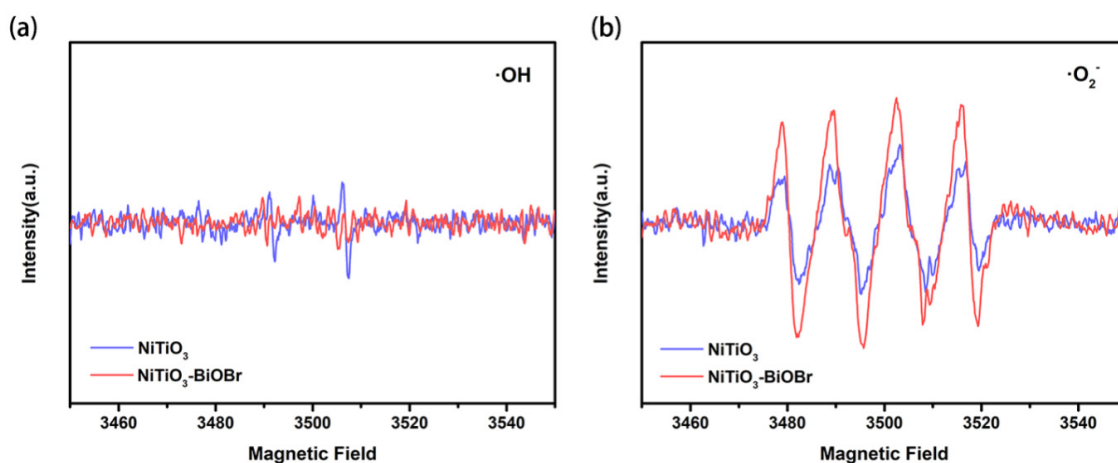


Figure 9. EPR spectra of (a) $\text{DMPO}\cdot\text{OH}$ and (b) $\cdot\text{O}_2^-$ over NiTiO_3 and $\text{NiTiO}_3\text{-BiOBr}$ composite with visible-light irradiation.

3.5.4. Band Position Determination

The band positions of NiTiO₃ and BiOBr were determined by both Mott–Schottky (MS) plots and their band gap energies. As shown in Figure 10, both NiTiO₃ and BiOBr belong to n-type semiconductors, as their MS plots exhibit positive slopes. The flat band energy (E_{fb}) of NiTiO₃ and BiOBr could be determined as -0.48 eV and -0.89 eV (vs. SCE), respectively, based on their intersections of the X-axis. The conduction band (CB) energy is usually ~ 0.1 eV more negative than E_{fb} for n-type semiconductors [33]. Consequently, the E_{CB} of NiTiO₃ and BiOBr are identified as -0.34 eV and -0.75 eV vs. NHE, respectively, according to the equation: NHE = 0.24 + SCE. Based on the E_g of NiTiO₃ (2.47 eV) and BiOBr (2.51 eV), the E_{VB} of NiTiO₃ and BiOBr are 2.13 eV and 1.76 eV ($E_{VB} = E_{CB} - E_g$), respectively.

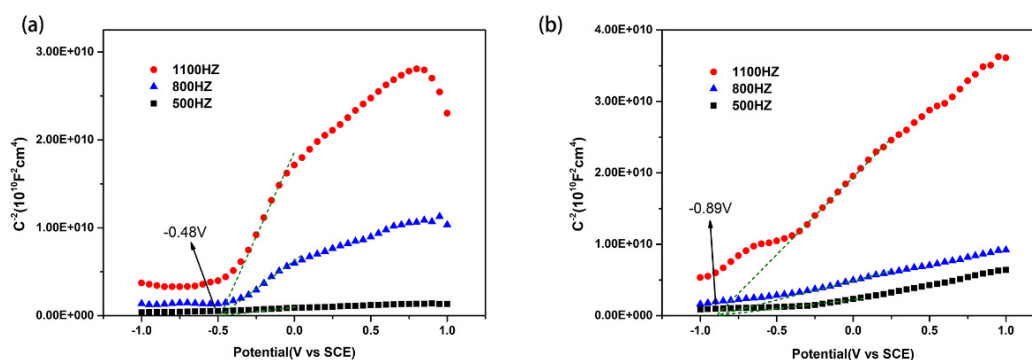


Figure 10. Mott–Schottky plots of (a) NiTiO₃ and (b) BiOBr.

3.6. Photocatalytic Mechanism of NiTiO₃-BiOBr Photocatalysts

Based on the above analysis, the transfer pathway of photoexcited carriers on the interface of the NiTiO₃-BiOBr heterojunction was discussed to clarify the photocatalytic degradation mechanism. As shown in Figure 11, electrons (e^-) on the VB of both NiTiO₃ and BiOBr would separately attain the corresponding light energy to jump to their CB under visible-light irradiation, leaving holes (h^+) on their VB. According to the CB and VB positions of the two semiconductors, the photo-induced carrier migration could follow the S-scheme transfer pathway (Figure 11a) [34,35] or type II transfer pathway (Figure 11b) [11,12]. Here, if the carriers follow the former, the e^- on the CB of NiTiO₃ would combine with the h^+ on the VB of BiOBr, thus inhibiting the recombination of e^- on CB of BiOBr and h^+ on the VB of NiTiO₃ and remaining their inherent redox capacity. This means that accumulating h^+ on the VB of NiTiO₃ in the composites could oxidize OH^- to generate more $\cdot OH$ than that in the single NiTiO₃. However, it is conflicted with the experimental results of the EPR (Figure 9a). Consequently, the S-scheme transfer pathway is excluded, and the conventional type II transfer pathway is proposed.

As illustrated in Figure 11b, the potential level difference between BiOBr and NiTiO₃ would lead to the transfer of e^- from BiOBr to NiTiO₃ and the transfer of h^+ in the opposite direction, resulting in the highly efficient separation of the carriers. The e^- accumulated on the CB of NiTiO₃ would reduce the adsorbed oxygen to generate a large quantity of $\cdot O_2^-$ due to their more negative potential than $E^0(O_2/\cdot O_2^-)$ (0.13 eV vs. NHE) [36], efficiently degrading RhB and TC. The accumulating h^+ on the VB of BiOBr could directly oxidize RhB. Nevertheless, they could not oxidize OH^- to $\cdot OH$ according to their lower potential than $E^0(\cdot OH/OH^-)$ (1.99 eV vs. NHE) [24], which is well in line with the EPR results. Consequently, the composites exhibited notably improved photodegradation efficiency for RhB and TC due to the high separation of photogenerated carriers benefiting from the type II heterojunctions with large interface areas. Additionally, the strengthened visible light absorption of the composites also causes an improvement in their photocatalytic efficiency.

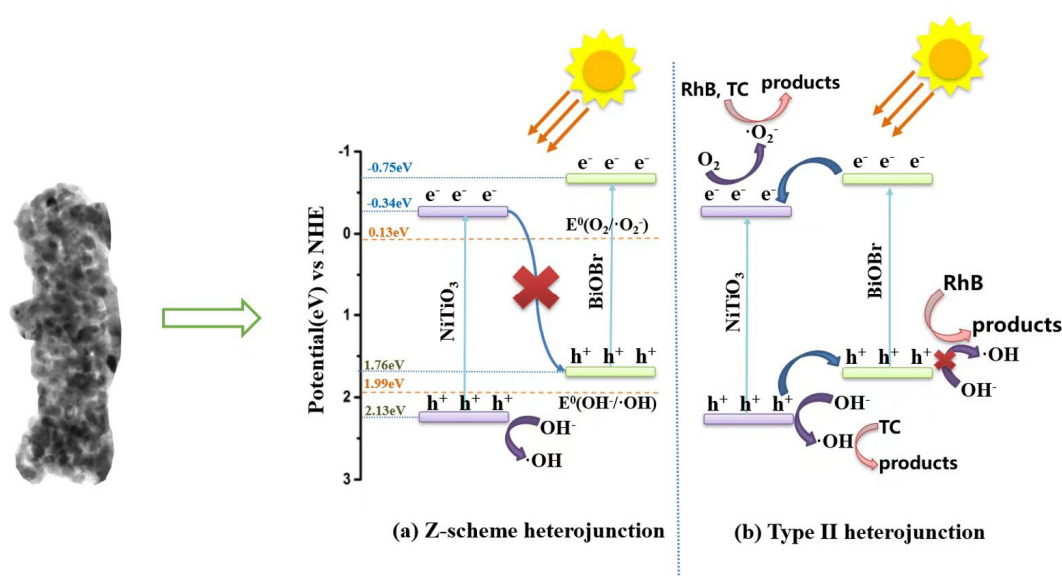


Figure 11. Proposed charge transfer pathway on the interface of heterojunction and photocatalytic mechanism of the NiTiO₃-BiOBr composites in degrading organic pollutants.

4. Conclusions

In this study, a series of novel binary NiTiO₃-BiOBr materials were synthesized via precipitation, calcination and hydrothermal methods in turn. As shown by various characterizations, BiOBr nanosheets were decorated on the NiTiO₃ nanoparticles, forming porous rod-like NiTiO₃-BiOBr heterojunctions with large interface area. The visible-light photodegradation capacity of the binary composites was significantly boosted compared with single NiTiO₃ and BiOBr. The optimum composite degraded 96.6% of RhB within 1.5 h (100% in 2 h) and 73.5% of TC within 3 h, which are 6.61 and 1.53 times those of NiTiO₃, respectively. In addition, it exhibited excellent photostability. The UV-Vis DRS spectroscopy and PL analysis indicate that the NiTiO₃-BiOBr heterojunctions strengthened visible-light absorption and notably facilitated the separation of photogenerated carriers, resulting in high photocatalytic activity. Considering the results of the free radical capture tests, EPR measurements and band position analysis, a feasible photodegradation mechanism of type-II heterojunction was proposed. This work provided a strategy for fabricating highly efficient NiTiO₃-based photocatalysts for degrading certain organic objects.

Author Contributions: Conceptualization, K.S.; Methodology, K.S.; Formal analysis, H.Z. and X.M.; Investigation, K.S. and M.L.; Resources, X.M. and W.L.; Data curation, M.L.; Writing—original draft, K.S.; Writing—review & editing, K.S. and H.Z.; Project administration, W.L. All authors have read and agreed to the published version of the manuscript.

Funding: The financial support provided by the Open Research Fund of State Key Laboratory of Multiphase Complex Systems (MPCS-2021-D-11).

Institutional Review Board Statement: Not applicable.

Informed Consent Statement: Not applicable.

Data Availability Statement: The authors confirm that the data supporting the findings of this study are available within the article.

Acknowledgments: We gratefully acknowledge the financial support provided by the Open Research Fund of State Key Laboratory of Multiphase Complex Systems (MPCS-2021-D-11).

Conflicts of Interest: The authors declare no conflict of interest.

References

1. Sun, K.Y.; Zhou, H.L.; Li, X.Y.; Ma, X.H.; Zhang, D.H.; Li, M.C. The novel 2-dimensional $\text{Bi}_2\text{MoO}_6\text{-Bi}_2\text{O}_3\text{-Ag}_3\text{PO}_4$ ternary photocatalyst with n-n-p heterojunction for enhanced degradation performance. *J. Alloys Compd.* **2022**, *913*, 165119. [\[CrossRef\]](#)
2. Ibrahim, I.; Belessiotis, G.; Antoniadou, M.; Kaltzoglou, A.; Sakellis, E.; Katsaros, F.; Sygellou, L.; Arfanis, M.; Salama, T.; Falaras, P. Silver decorated $\text{TiO}_2/\text{g-C}_3\text{N}_4$ bifunctional nanocomposites for photocatalytic elimination of water pollutants under UV and artificial solar light. *Results Eng.* **2022**, *14*, 100470. [\[CrossRef\]](#)
3. Fu, K.; Pan, Y.; Ding, C.; Shi, J.; Deng, H. Photocatalytic degradation of naproxen by $\text{Bi}_2\text{MoO}_6/\text{g-C}_3\text{N}_4$ heterojunction photocatalyst under visible light: Mechanisms, degradation pathway, and DFT calculation. *J. Photochem. Photobiol. A Chem.* **2021**, *412*, 113235. [\[CrossRef\]](#)
4. Li, Q.Q.; Zhao, W.L.; Zhai, Z.C.; Ren, K.X.; Wang, T.Y.; Guan, H.; Shi, H.F. 2D/2D $\text{Bi}_2\text{MoO}_6/\text{g-C}_3\text{N}_4$ S-scheme heterojunction photocatalyst with enhanced visible-light activity by Au loading. *J. Mater. Sci. Technol.* **2020**, *56*, 216–226. [\[CrossRef\]](#)
5. Falara, P.; Ibrahim, I.; Zourou, A.; Sygellou, L.; Sanchez, D.E.; Romanos, G.; Givalou, L.; Antoniadou, M.; Arfanis, M.; Han, C.; et al. Bi-functional photocatalytic heterostructures combining titania thin films with carbon quantum dots (C-QDs/ TiO_2) for effective elimination of water pollutants. *Environ. Sci. Pollut. Res. Int.* **2023**, 1–16. [\[CrossRef\]](#) [\[PubMed\]](#)
6. Li, Y.B.; Wang, G.R.; Wang, Y.B.; Jin, Z.L. Phosphating 2D CoAl LDH anchored on 3D self-assembled NiTiO_3 hollow rods for efficient hydrogen evolution. *Catal. Sci. Technol.* **2020**, *10*, 2931–2947. [\[CrossRef\]](#)
7. Liu, J.; Li, X.H.; Han, C.H.; Zhou, X.J.; Li, X.W.; Liang, Y.; Liu, S.; Shao, C.L.; Liu, Y.C. Ternary $\text{NiTiO}_3/\text{g-C}_3\text{N}_4\text{-Au}$ nanofibers with a synergistic Z-scheme core@shell interface and dispersive Schottky contact surface for enhanced solar photocatalytic activity. *Mater. Chem. Front.* **2021**, *5*, 2730–2741. [\[CrossRef\]](#)
8. Trang, N.T.T.; Khang, D.M.; Dung, D.D.; Trung, N.N.; Phuong, N.T.; Bac, L.H. Synthesis of Ilmenite NiTiO_3 Rods and Effect of pH on Rhodamine B Textile Dye Degradation under LED Visible-Light Irradiation. *J. Electon. Mater.* **2021**, *50*, 7188–7197. [\[CrossRef\]](#)
9. Absalan, Y.; Bratchikova, I.; Kovalchukova, O. Accurate investigation to determine the best conditions for using NiTiO_3 for bromophenol blue degradation in the environment under UV-vis light based on concentration reduction and to compare it with TiO_2 . *Environ. Nanotechnol. Monit. Manag.* **2017**, *8*, 244–253. [\[CrossRef\]](#)
10. Wang, H.; Yuan, X.Z.; Wang, H.; Chen, X.H.; Wu, Z.B.; Jiang, L.B.; Xiong, W.P.; Zhang, Y.X.; Zeng, G.M. One-step calcination method for synthesis of mesoporous $\text{g-C}_3\text{N}_4/\text{NiTiO}_3$ heterostructure photocatalyst with improved visible light photoactivity. *RSC Adv.* **2015**, *5*, 95643–95648. [\[CrossRef\]](#)
11. Peng, D.X.; Wang, Y.T.; Shi, H.F.; Jiang, W.; Jin, T.; Jin, Z.H.; Chen, Z. Fabrication of novel $\text{Cu}_2\text{WS}_4/\text{NiTiO}_3$ heterostructures for efficient visible-light photocatalytic hydrogen evolution and pollutant degradation. *J. Colloid Interface Sci.* **2022**, *613*, 194–206. [\[CrossRef\]](#) [\[PubMed\]](#)
12. Li, H.Y.; Wang, G.R.; Gong, H.M.; Jin, Z.L. Phosphated 2D MoS_2 nanosheets and 3D NiTiO_3 nanorods for efficient photocatalytic hydrogen evolution. *ChemCatChem* **2020**, *12*, 5492–5503. [\[CrossRef\]](#)
13. Li, Z.Z.; Zhang, H.G.; Wang, L.; Meng, X.C.; Shi, J.J.; Qi, C.X.; Zhang, Z.S.; Feng, L.J.; Li, C.H. 2D/2D $\text{BiOBr}/\text{Ti}_3\text{C}_2$ heterojunction with dual applications in both waterdetoxification and water splitting. *J. Photochem. Photobiol. A Chem.* **2020**, *386*, 112099. [\[CrossRef\]](#)
14. Li, X.B.; Xiong, J.; Gao, X.M.; Ma, J.; Chen, Z.; Kang, B.B.; Liu, J.Y.; Li, H.; Feng, Z.J.; Huang, J.T. Novel BP/ BiOBr S-scheme nano-heterojunction for enhanced visible-light photocatalytic tetracycline removal and oxygen evolution activity. *J. Hazard. Mater.* **2020**, *387*, 121690. [\[CrossRef\]](#)
15. Liu, H.; Zhou, H.L.; Liu, X.T.; Li, H.D.; Ren, C.J.; Li, X.Y.; Li, W.J.; Lian, Z.Q.; Zhang, M. Engineering design of hierarchical $\text{g-C}_3\text{N}_4/\text{Bi}/\text{BiOBr}$ ternary heterojunction with Z-scheme system for efficient visible-light photocatalytic performance. *J. Alloys Compd.* **2019**, *798*, 741–749. [\[CrossRef\]](#)
16. Liu, K.; Zhang, H.B.; Muhammad, Y.; Fu, T.; Tang, R.; Tong, Z.F.; Wang, Y. Fabrication of n-n isotype $\text{BiOBr-Bi}_2\text{WO}_6$ heterojunctions by inserting Bi_2WO_6 nanosheets onto BiOBr microsphere for the superior photocatalytic degradation of Ciprofloxacin and tetracycline. *Sep. Purif. Technol.* **2021**, *274*, 118992–119005. [\[CrossRef\]](#)
17. Hao, L.; Ju, P.; Zhang, Y.; Sun, C.J.; Dou, K.P.; Liao, D.K.; Zhai, X.F.; Lu, Z.X. Novel plate-on-plate hollow structured $\text{BiOBr}/\text{Bi}_2\text{MoO}_6$ p-n heterojunctions: In-situ chemical etching preparation and highly improved photocatalytic antibacterial activity. *Sep. Purif. Technol.* **2022**, *298*, 121666–121682. [\[CrossRef\]](#)
18. Fu, S.; Yuan, W.; Liu, X.M.; Yan, Y.H.; Liu, H.P.; Li, L.; Zhao, F.Y.; Zhou, J.G. A novel 0D/2D WS_2/BiOBr heterostructure with rich oxygen vacancies for enhanced broad-spectrum photocatalytic performance. *J. Colloid Interface Sci.* **2020**, *569*, 150–163. [\[CrossRef\]](#)
19. Yan, Q.S.; Guo, Z.Y.; Wang, P.Y.; Cheng, Y.N.; Wu, C.Y.; Zuo, H.R. Facile construction of 0D/2D $\text{In}_2\text{O}_3/\text{Bi}_2\text{WO}_6$ Z-scheme heterojunction with enhanced photocatalytic activity for antibiotics removal. *J. Alloys Compd.* **2023**, *937*, 168362. [\[CrossRef\]](#)
20. Qu, Y.; Zhou, W.; Ren, Z.Y.; Du, S.C.; Meng, X.Y.; Tian, G.H.; Pan, K.; Wang, G.F.; Fu, H.G. Facile preparation of porous NiTiO_3 nanorods with enhanced visible-light-driven photocatalytic performance. *J. Mater. Chem.* **2012**, *22*, 16471–16476. [\[CrossRef\]](#)
21. Kim, S.R.; Jo, W.K. Application of a photostable silver-assisted Z-scheme NiTiO_3 nanorod/ $\text{g-C}_3\text{N}_4$ nanocomposite for efficient hydrogen generation. *Int. J. Hydrogen Energy* **2019**, *44*, 801–808. [\[CrossRef\]](#)
22. Shi, Y.Q.; Xiong, X.Y.; Ding, S.P.; Liu, X.F.; Jiang, Q.Q.; Hu, J.C. In-situ topotactic synthesis and photocatalytic activity of plate-like $\text{BiOCl}/2\text{D networks Bi}_2\text{S}_3$ heterostructures. *Appl. Catal. B Environ.* **2018**, *220*, 570–580. [\[CrossRef\]](#)
23. Liu, H.J.; Wang, B.J.; Chen, M.; Zhang, H.; Peng, J.B.; Ding, L.; Wang, W.F. Simple synthesis of $\text{BiOAc}/\text{BiOBr}$ heterojunction composites for the efficient photocatalytic removal of organic pollutants. *Sep. Purif. Technol.* **2021**, *261*, 118286. [\[CrossRef\]](#)

24. Qu, X.F.; Liu, M.H.; Zhang, W.X.; Sun, Z.; Meng, W.; Shi, L.; Du, F.L. A facile route to construct $\text{NiTiO}_3/\text{Bi}_4\text{NbO}_8\text{Cl}$ heterostructures for enhanced photocatalytic water purification. *J. Mater. Sci.* **2020**, *55*, 9330–9342. [[CrossRef](#)]
25. Pham, T.T.; Nguyen-Huy, C.; Shin, E.W. NiTiO_3 /reduced graphene oxide materials synthesized by a two-step microwave-assisted method. *Mater. Lett.* **2016**, *184*, 38–42. [[CrossRef](#)]
26. Lakhera, S.K.; Hafeez, H.Y.; Veluswamy, P.; Ganesh, V.; Khan, A.; Ikeda, H.; Neppolian, B. Enhanced photocatalytic degradation and hydrogen production activity of in situ grown TiO_2 coupled NiTiO_3 nanocomposites. *Appl. Surf. Sci.* **2018**, *449*, 790–798. [[CrossRef](#)]
27. Jin, Y.M.; Shen, X.F.; Liu, Z.X.; Wang, Z.J.; Zhu, B.; Xu, P.F.; Luo, L.; Zhang, L.S. Synthesis of $\text{NiTiO}_3\text{-Bi}_2\text{MoO}_6$ core-shell fiber-shaped heterojunctions as efficient and easily recyclable photocatalysts. *New J. Chem.* **2018**, *42*, 411–419. [[CrossRef](#)]
28. Zhang, Y.; Gu, J.; Murugananthan, M.; Zhang, Y.R. Development of novel $\alpha\text{-Fe}_2\text{O}_3/\text{NiTiO}_3$ heterojunction nanofibers material with enhanced visible-light photocatalytic performance. *J. Alloys Compd.* **2015**, *630*, 110–116. [[CrossRef](#)]
29. Zarazúa-Morín, M.E.; Galindo-Luna, A.S.; Gallegos-Sánchez, V.J.; Zermeno-Resendiz, B.B.; Torres-Martínez, L.M. Novel hydrothermal-assisted microwave synthesis of $\text{NiTiO}_3/\text{ZnO}$ and sonophotocatalytic effect for degradation of rhodamine B. *Top. Catal.* **2022**, *65*, 1182–1190. [[CrossRef](#)]
30. Wang, Z.Y.; Peng, J.W.; Feng, X.; Ding, Z.X.; Li, Z.H. Wide spectrum responsive $\text{CdS}/\text{NiTiO}_3/\text{CoS}$ with superior photocatalytic performance for hydrogen evolution. *Catal. Sci. Technol.* **2017**, *7*, 2524–2530. [[CrossRef](#)]
31. Wang, Z.L.; Huo, Y.; Zhang, J.F.; Lu, C.; Dai, K.; Liang, C.H.; Zhu, G.P. Facile preparation of two-dimensional $\text{Bi}_2\text{MoO}_6@\text{Ag}_2\text{MoO}_4$ core-shell composite with enhanced visible light photocatalytic activity. *J. Alloys Compd.* **2017**, *729*, 100–108. [[CrossRef](#)]
32. Hu, T.P.; Yang, Y.; Dai, K.; Zhang, J.F.; Liang, C.H. A novel Z-scheme $\text{Bi}_2\text{MoO}_6/\text{BiOBr}$ photocatalyst for enhanced photocatalytic activity under visible light irradiation. *Appl. Surf. Sci.* **2018**, *456*, 473–481. [[CrossRef](#)]
33. Li, H.Y.; Wang, G.R.; Gong, H.M.; Jin, Z.L. Hollow Nanorods and Amorphous Co_9S_8 Quantum Dots Construct S-Scheme Heterojunction for Efficient Hydrogen Evolution. *J. Phys. Chem. C* **2021**, *125*, 648–659. [[CrossRef](#)]
34. Li, B.F.; Wang, W.J.; Zhao, J.W.; Wang, Z.Y.; Su, B.; Hou, Y.D.; Ding, Z.X.; Ong, W.J.; Wang, S.B. All-solid-state direct Z-scheme $\text{NiTiO}_3/\text{Cd}_{0.5}\text{Zn}_{0.5}\text{S}$ heterostructures for photocatalytic hydrogen evolution with visible light. *J. Mater. Chem. A* **2021**, *9*, 10270–10276. [[CrossRef](#)]
35. Pham, T.T.; Shin, E.W. Inhibition of charge recombination of NiTiO_3 photocatalyst by the combination of Mo-doped impurity state and Z-scheme charge transfer. *Appl. Surf. Sci.* **2020**, *501*, 143992. [[CrossRef](#)]
36. Tang, C.N.; Liu, E.Z.; Fan, J.; Hu, X.Y.; Ma, Y.N.; Wan, J. Graphitic- C_3N_4 -hybridized Ag_3PO_4 tetrahedron with reactive{111} facets to enhance the visible-light photocatalytic activity. *RSC Adv.* **2015**, *5*, 91979–91987. [[CrossRef](#)]

Disclaimer/Publisher’s Note: The statements, opinions and data contained in all publications are solely those of the individual author(s) and contributor(s) and not of MDPI and/or the editor(s). MDPI and/or the editor(s) disclaim responsibility for any injury to people or property resulting from any ideas, methods, instructions or products referred to in the content.